Supporting Information

Highly stable manganese oxide cathode material enabled by

Grotthuss topochemistry for aqueous zinc ion batteries

Fangjia Zhao,[a] Jianwei Li,[b] Arunabhiram Chutia,[c] Longxiang Liu,[a] Liqun Kang,[d] Feili Lai,[e] Haobo Dong,[a]

Xuan Gao,[a] Yeshu Tan,[a] Tianxi Liu,[f] Ivan P. Parkin*[a] and Guanjie He*[a]

[a] *Department of Chemistry, University College London, 20 Gordon Street, London WC1H 0AJ, UK. E-Mail: i.p.parkin@ucl.ac.uk; g.he@ucl.ac.uk*

[b] *Key Laboratory of Comprehensive and Highly Efficient Utilization of Salt Lake Resources, Qinghai Province Key Laboratory of Resources and Chemistry of Salt Lakes, Qinghai Institute of Salt Lakes, Chinese Academy of Sciences, Xining, Qinghai 810008, P. R. China.*

[c] *School of Chemistry, University of Lincoln, Brayford Pool, Lincoln, LN6 7TS, UK*

[d] *Max Planck Institute for Chemical Energy Conversion, Stiftstrasse 34-36, 45470 Mülheim an der Ruhr, Germany*

[e] *Department of Chemistry, KU Leuven Celestijnenlaan 200F, Leuven 3001, Belgium*

[f] *School of Chemical and Material Engineering, Jiangnan University, No. 1800, Lihu Avenue, Wuxi 214122, China*

Experimental section

S1. Material synthesis

The following chemicals are used as received without further purification: Potassium permanganate (Sigma-Aldrich, ACS reagent, ≥ 99.0%); Manganese (II) nitrate tetrahydrate (Fisher chemical, AR ≥ 98.0%); Nickel (II) nitrate hexahydrate (Sigma-Aldrich, ACS reagent, ≥ 99.0%); Ammonium chloride (Sigma-Aldrich, ACS reagent, ≥95%); Zinc trifluoromethanesulfonate (Sigma-Aldrich, ACS reagent, 98%); Manganese bis(trifluoromethanesulfonate) (Sigma-Aldrich, ACS reagent, ≥98%); Poly(vinylidene fluoride) (Sigma-Aldrich, average Mw ~534,000 by GPC, powder) N-methyl-2-pyrrolidone (Sigma-Aldrich, ACS reagent, ≥99.0%).

Cation-defective $NiMn_3O_7$ cathode material V_m-NMO was synthesised according to the previous literature.[1] $KMnO_4$ aqueous solution (0.04 M, 18 mL), NH_4Cl aqueous solution (0.04 M, 18 mL) and $Ni(NO_3)_2$ aqueous solution (1 M, 4 mL) were added stage by stage and vigorously stirred for 25 min. Then the acquired mixture was shifted in an autoclave and heated in an electric oven at 200 °C for 24 h. The resulting precursor was gathered and washed (deionised water three times and ethanol one time), then dried in an oven at 60 °C overnight. NMO was synthesised following the same process without the addition of NH_4Cl aqueous solution. V_n-NMO, V_o-NMO and V_p-NMO were synthesised following the same heating process by adjusting the addition of NH_4Cl aqueous solution to 0.08 M (18 mL), 0.4 M (18 mL) and 1 M (18 mL).

S2. Material characterisation

X-ray diffraction (XRD) patterns were obtained by a STOE SEIFERT diffractometer with detected angular range of 2° < 2θ < 40° with a Mo X-ray radiation source. The morphology and chemical states of the as-prepared materials were evaluated by scanning electron microscope (SEM, Jeol 7600F SEM), transmission electron microscopy (TEM JEOL, JEM-2100 and ARM200F) and X-ray photoelectron spectroscopy (XPS, Thermo Scientific K-alpha photoelectron spectrometer) analysis, respectively. Data processing of XPS results was conducted using CasaXPS software with the calibration of adventitious carbon binding energy at 284.8 eV. Raman and FT-IR data were obtained on a Raman Spectroscopy (Renishaw Raman microscope spectrometer with a laser wavelength of 514.5 nm) and Attenuated Total Reflectance Fourier transform infrared spectroscopy (ATR-FTIR, BRUKER, platinum-ATR). The mass change during annealing was recorded by a Thermogravimetric analyser (TGA) (PerkinElmer TGA 4000 System). The mass of the active materials was weighed accurately by an analytical balance (Ohaus; δ= 0.01 mg). Crystallographic structures were stimulated via VESTA software by applying standard ICSD CIF documents. The Mn, Ni and Zn K-edges X-ray Absorption Spectra of electrode plates were collected at B18@Diamond Light Source. The monochromatic beam between 6.35 keV and 10.55 keV (k_{max} = 16) was introduced through a bending magnet and Pt-coated Si(111) double crystal monochromator. The beam size at the sample was approx. 1.0 x 1.0 mm2 (V x H) and the photon flux was ~10^{11} ph/s (no attenuation). The XAFS spectra were collected in transmission mode, and the intensity of the incident beam (I0) and the transmitted beam (It) was monitored by ionisation chambers (filled with a mixture of He and N2). The sample was made of electrode carbon paper (D:8mm) and was cut into four pieces, stacked together, sealed with Kapton tape, and mounted on the sample rack. The XAFS measurements were performed under R.T. The XAFS of each sample was measured two times and merged to improve the signal-noise ratio. Mn, Ni, and Zn foil were measured simultaneously for each sample as a reference for energy calibration. The NEXAFS experiment was performed at the B07-B beamline of Diamond Light Source (UK).[1] NEXAFS measurements of O K-edge, Mn L-edge, and Ni L-edge were performed in total electron yield (TEY) mode in the ES-2 end station for Ambient Pressure NEXAFS.[2] The pristine, charged, and discharged electrode, as well as Mn_2O_3 and MnO_2 powder reference, were dispersed on carbon tape by pressing, which ensured good conductivity. The samples were illuminated by an incident beam sourced from a bending magnet and plane grating monochromator (PGM) with a spot size of approx. 200 μm × 200 μm. The pressure in the specimen chamber is controlled at $1 × 10^{-7}$ mbar. Three repetitions of NEXAFS spectrum were collected and merged to improve the signal-to-noise ratio for every edge. The energy resolution was set to 0.1 eV for each repetition. The energy shifts of O K-edge, Mn L-edge, and Ni L-edge were calibrated by the spectra of standard Mn_2O_3 and NiO, respectively. The NEXAFS spectra were divided by the incident beam intensity. X-ray Absorption Spectroscopy data processing and analysis using Demeter.

S3. Electrochemical measurements

The electrochemical performance of $NiMn_3O_7$ was tested by assembling them into coin cells. Typically, 70 wt% of

as-prepared was mixed with 20 wt% of Carbon black Super-P and 10 wt% of poly(vinylidene fluoride) (PVDF) in N-methylpyrrolidone (NMP) solvent. The resulting slurry was then deposited onto carbon paper and vacuum dried for 8 h under 80 °C to form the cathode part, which was matched with 500 um thickness zinc plate anode to completely form a coin cell configuration using 3 M $Zn(Otf)_2$, 0.2 M $Mn(Otf)_2$ electrolyte and Whatman GF/A glass fibre as the separator.[3] With a diameter of 1.4 cm, the loading mass of cut discs of electrodes is between 1.0 and 2.5 mg cm^{-1}. All battery performances were characterised on the Neware battery system, and the cyclic voltammetry curves profiles were performed within 0.9–1.9 V (vs. Zn^{2+}/Zn). Cyclic voltammetry and EIS testing were performed with VMP3 Biotech potentiostat.

Note 1: Estimation of the capacitive and diffusion-controlled contributions

To distinguish quantitatively the capacitive and diffusion-controlled contributions to the current, cyclic voltammetry curves were recorded at different sweep rates. In general, there is a relationship between the measured peak current (i) and sweep rate (v) in a CV scan, which follows the power law:

$$i = av^b$$

alternatively, $\log(i) = \log(a) + b \times \log(v)$

The b-value can therefore be obtained by fitting the log(i) versus log(v) slope. A b value of 0.5 suggests a diffusion-controlled behaviour, while a b value of 1.0 indicates a capacitive behaviour. The capacitive contribution and the diffusion-controlled contribution can be further distinguished. By quantitatively assuming that the current (i) is a combination of the capacitive and the diffusion-controlled processes:

$$i = k_1 v + k_2 v^{\frac{1}{2}}$$

k_1 can be used to estimate capacitive and diffusion-controlled contributions.

Note 2: Study on Galvanostatic Intermittent Titration Technique (GITT)

GITT was employed to establish the thermodynamic voltage-composition relationship, which is consistent with the equilibrium phase diagram.[4, 5] The diffusion coefficients of Zn^{2+} ions were evaluated from the GITT data. In the GITT process, the transient voltage induced by the application of a current pulse is studied as a function of time. The GITT testing undergoes charge/discharge for 15 cycles under 0.1 A g^{-1} to reach a stable state. Subsequently, a galvanostatic pulse of 30 mA g^{-1} was applied to the assembled coin cell for 20 minutes duration, after which following with a 2 hours relaxation open circuit step for the equilibrium phase (defined as < 2 mV h^{-1}). These steps repeated until the batteries reached fully charged/discharged states.

The diffusion coefficients of the charge carriers follow the equation:

$$D_{charge\ carriers} = \frac{4}{\pi}\left(\frac{n_M V_M}{S}\right)^2 \left[\frac{\Delta E_s}{\tau\left(\frac{dE_\tau}{d\sqrt{\tau}}\right)}\right]^2 \left(\tau \ll \frac{L^2}{D_{charge\ carriers}}\right)$$

Where τ stands for the dwell time of the constant current pulse (set as 20 min in this research); S corresponds to the interface area of cathode material and electrolyte (unit: cm^{-2}, refers to the geometric area of the electrode); n_M and V_M are the moles (unit: mol) of $NiMn_3O_7$ and molar volume (unit: $cm^3\ mol^{-1}$), respectively; ΔE_s and ΔE_τ are the shift in steady-state voltage and the total cell voltage after applying a current pulse in a single-step GITT testing, eliminating the i_R drop, respectively. L refers to the cathode thickness. With the condition that the variation of the

cell voltage (ΔE_τ) is found to have a linear relationship with $\tau^{1/2}$, the above equation can be simplified into the following equation:

$$D_{charge\ carriers} = \frac{4}{\pi\tau}\left(\frac{n_M V_M}{S}\right)^2 \left[\frac{\Delta E_s}{\Delta E_\tau}\right]^2$$

S4. Computational details

All the density functional theory (DFT) calculations were performed using the Vienna Ab-initio Simulation package (VASP)[6, 7]. We used the projector augmented wave (PAW) method, with the plane-wave cut-off of 420 eV for the expansion of the wave functions, which provided bulk total energies converged to within 10^{-5} eV[8]. For the structural optimisation, we chose a convergence criterion of 0.01eV/A, and we used the Perdew-Burke-Ernzerhof (PBE) generalised gradient approximation (GGA) as the exchange-correlation functional[9, 10]. A gamma-centred 4x4x1 Monkhurst-Pack (MP) grid was used. The ideal $NiMn_2O_3$(100) models with three $NiMn_3O_7$ layers with water molecules in between them were modelled from the optimised unit cells with lattice parameters of a=7.552 Å (Exp.: 7.514 Å), b=6.540 Å (Exp.: 6.507 Å) and c=20.623 Å (Exp.: 20.520 Å). As shown in Figure 4 (a), the two top $NiMn_3O_7$ layers along with the water molecules in between them were relaxed and the bottom layers were fixed to mimic the bulk of the structure. A vacuum of ~15 Å was inserted along the surface's normal direction, which is sufficient to eliminate spurious interaction with the neighbouring image slabs. The dipole moment due to the presence of species was accounted for by using the methods of Neugebauer et al.[11, 12]. In this study, we also employed Grimme's dispersion correction (DFT+D3), as dispersion force might be significant for this system[13]. In previous studies, it has been reported that the localisation of electrons in d-orbitals of Mn^{4+} and Ni^{2+} ions is correctly represented by the Hubbard parameter (U_{eff}) of 4.0 eV and 5.3 eV, respectively[14]. Therefore, in this study, we have used U_{eff} of 4.0 eV, 5.3 eV and 0 eV, respectively, for the d-orbitals of Mn^{4+} and Ni^{2+} ions and p-orbital for O^{2-} ions. The adsorption energies (E_{ad}) of the proton on the $NiMn_2O_3$(100) surface were evaluated using equation (1).

$$E_{ad} = E_{H/NMO} - E_{NMO} - E_H \qquad\qquad (1)$$

where $E_{H/NMO}$ is the total energy of the proton adsorbed on the $NiMn_2O_3$(100) surface, E_{NMO} is the total energy of the relaxed pristine $NiMn_2O_3$(100) surface and E_H is the total energy of a hydrogen atom in the gas phase. To obtain $E_{H/NMO}$, the adsorption of the H-atom was allowed on various sites on the $NiMn_2O_3$(100) surface with and without Mn^{4+} defects, which includes a water molecule present between the $NiMn_2O_3$ layers in an O-atom of the $NiMn_2O_3$ layer and on the Mn^{4+} ions. The atomic charges were calculated using the Bader charge analysis as implemented by Henkelman and co-workers[15]. The VESTA package was used for visualisation of the optimised structures and to measure the interatomic distances, bond angles and dihedral angles[16, 17].
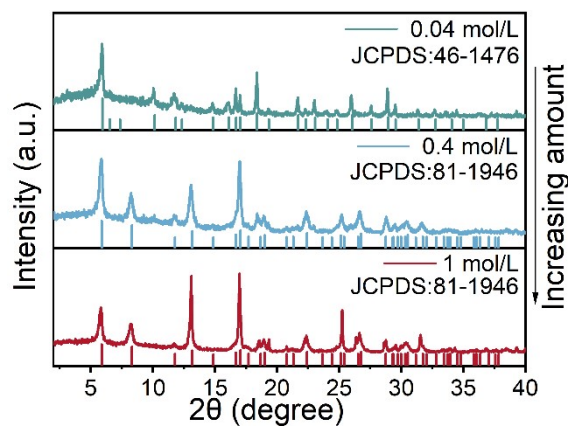
Fig. S1 XRD profiles of cathode material with different NH$_4$Cl adding amounts during the synthesis process.
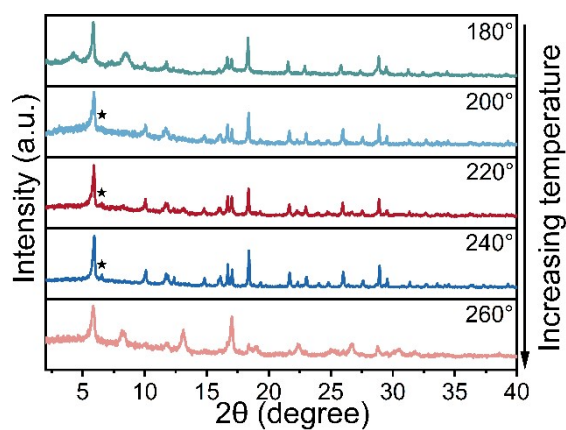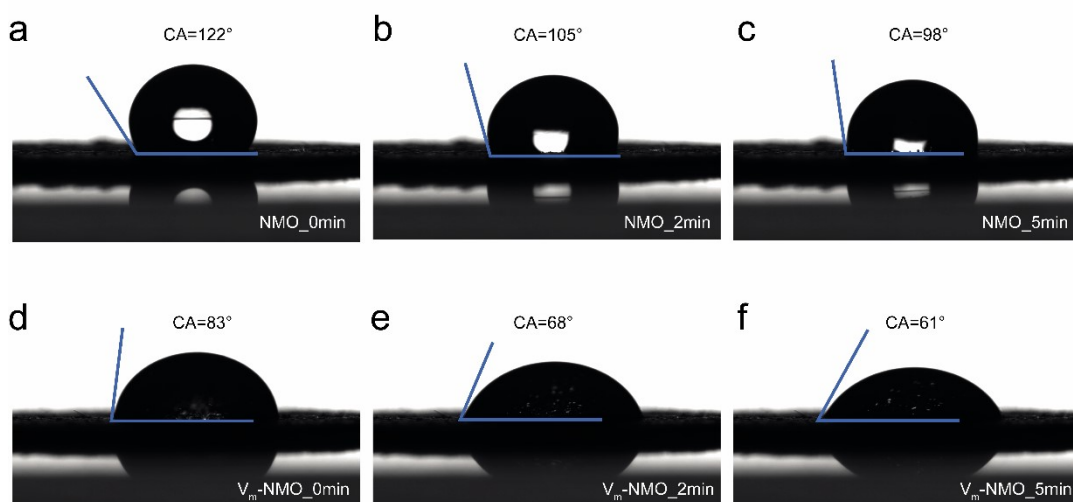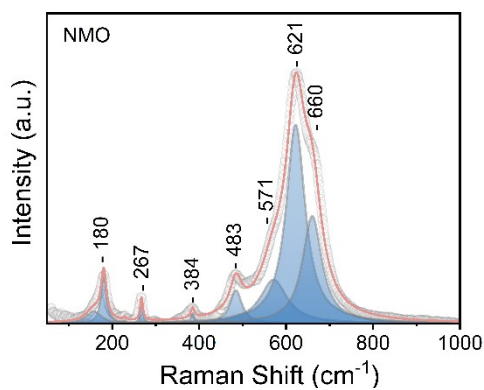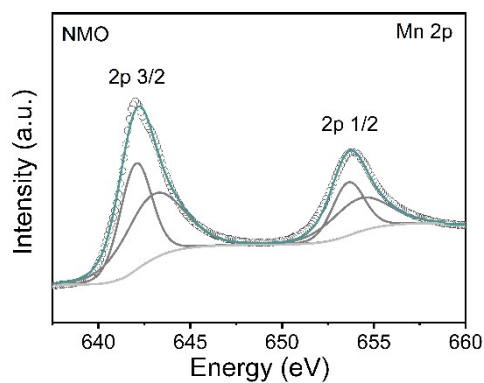

Fig. S2 XRD profiles of cathode material synthesised with different temperature conditions.
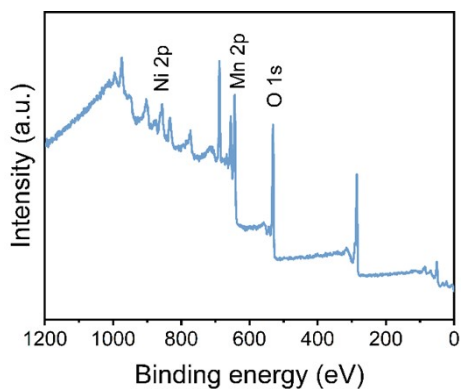
Fig. S3 Images of contact angles at 0, 2, 6 minutes of the 3 M Zn (OTf)$_2$ electrolyte on V$_m$-NMO electrode (a-c) and NMO electrode (d-f).
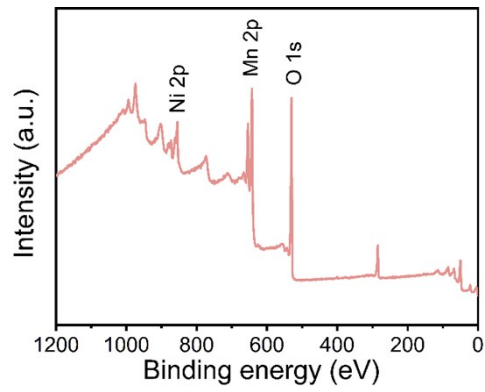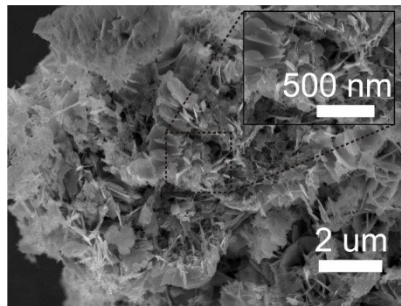

Fig.S4 Raman Spectra of NMO.
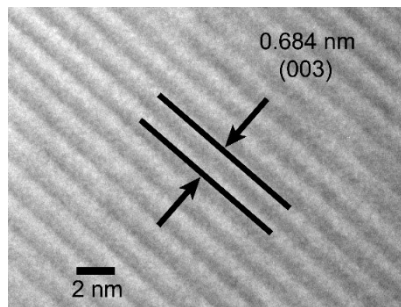

Fig.S5 XPS Mn 2p Spectra of NMO.

Fig.S6 XPS survey of V$_m$-NMO.

Fig.S7 XPS survey of NMO.

Fig.S8 SEM profile of V_m-NMO cathode materials.

Fig.S9 TEM profile of V_m-NMO cathode materials with lattice distance.
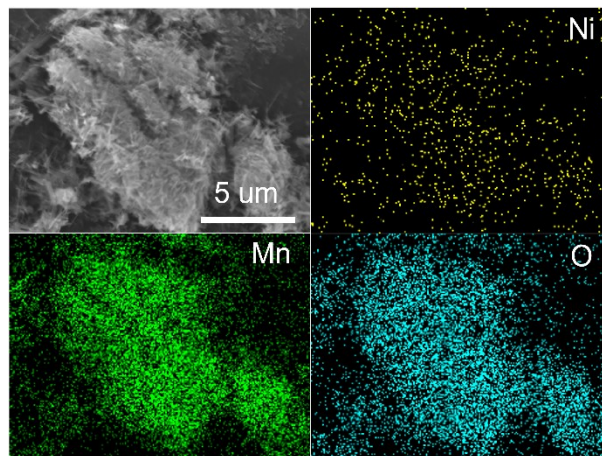
Fig.S10 SEM elemental mapping of V_m-NMO cathode materials.
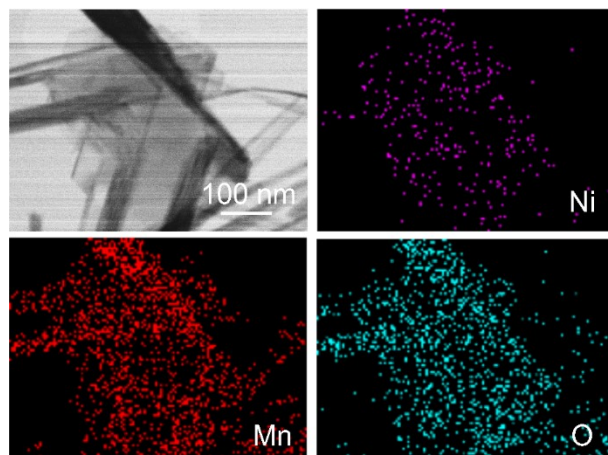
Fig.S11 TEM elemental mapping of V$_m$-NMO cathode materials.
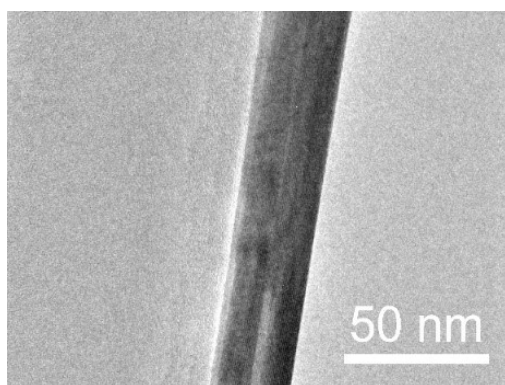
Fig.S12 TEM image of NMO cathode materials.
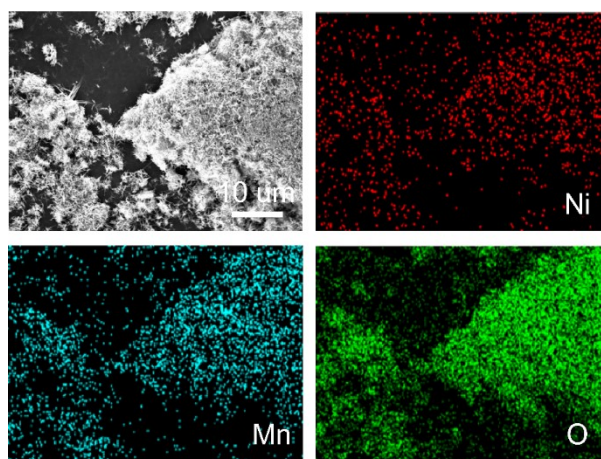
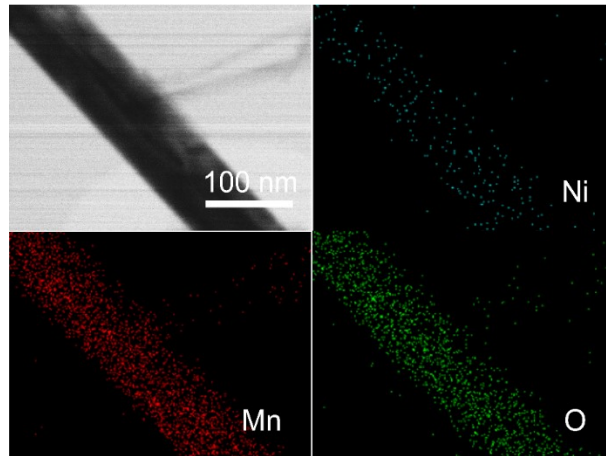**Fig.S13** SEM elemental mapping of NMO cathode materials.
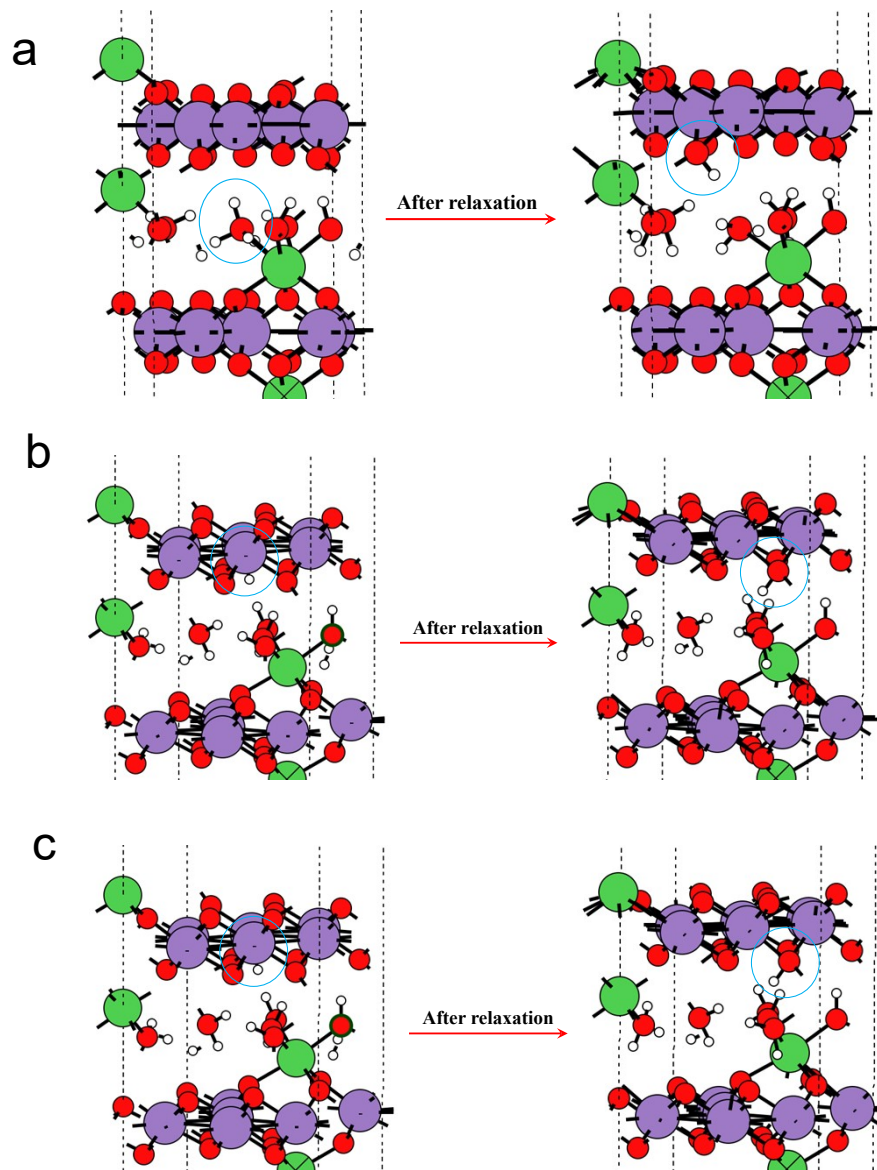
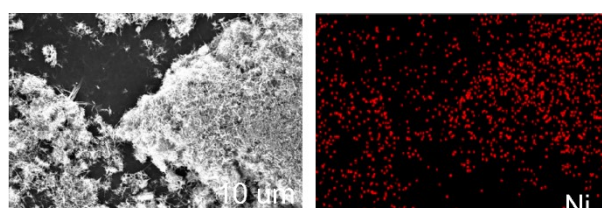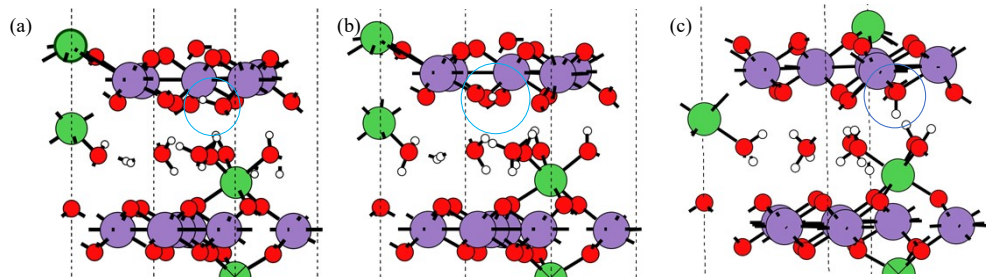**Fig.S14** TEM elemental mapping of NMO cathode materials.

Fig. S15 Adsorption of proton (**a**) on inter-layer water molecules, (**b**) on Mn^{4+} ion and (**c**) on O^{2-} ions of the $NiMn_3O_7$ layer.

Fig.S16 Fully relaxed geometries of proton (**a**) on the O^{2-} ion, which migrated from the Mn^{4+} defect site, (**b**) on an O^{2-} ion next to the defect site, and (**c**) on an O^{2-} ion away from the Mn^{4+} defect site.

Position 1	Position 2	Position 3
E_{ad}= -5.071 eV	E_{ad}= -5.072 eV	E_{ad}= -4.028 eV
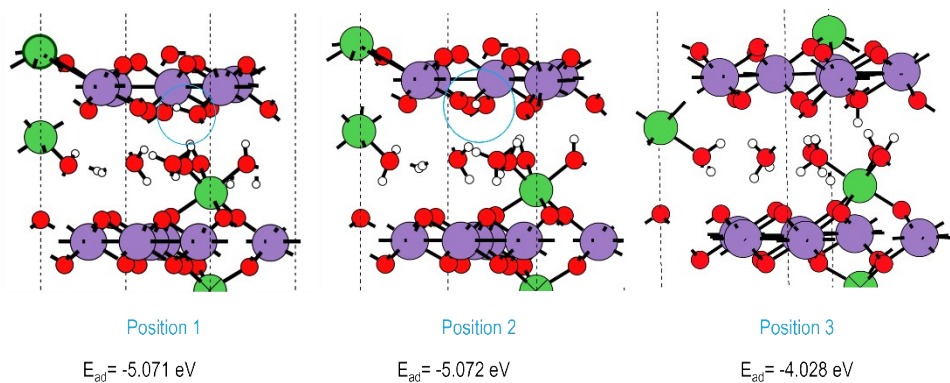
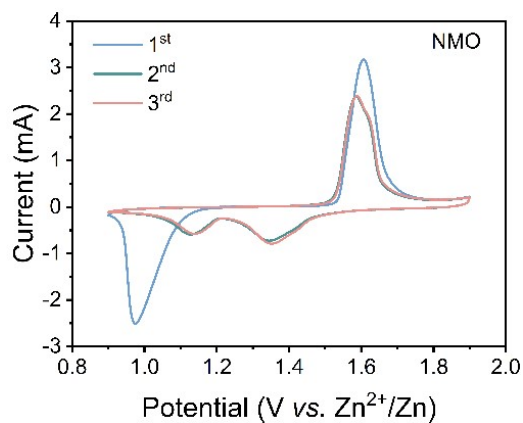**Fig.S17** Adsorption energies in different sites with an Mn^{4+} defect.

Fig.S18 CV profile of NMO.

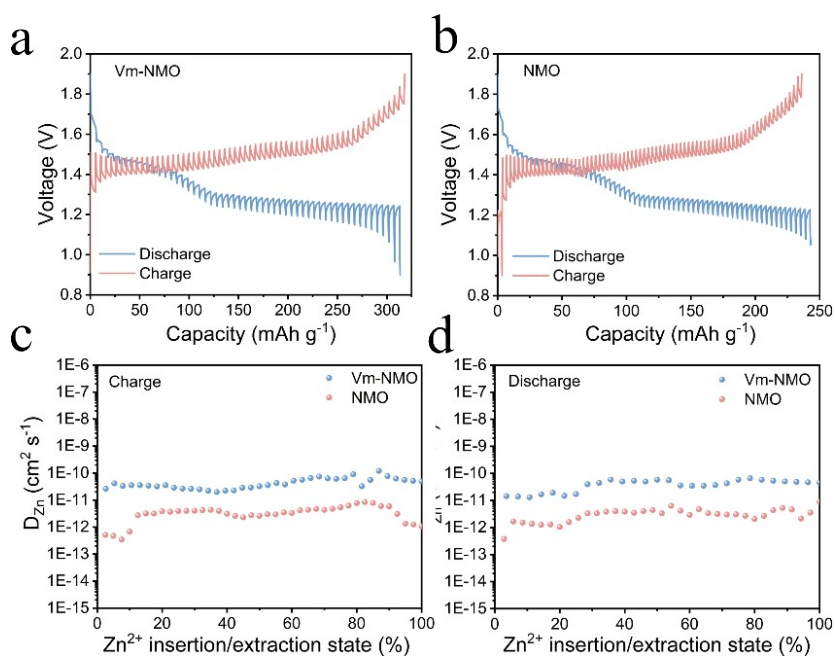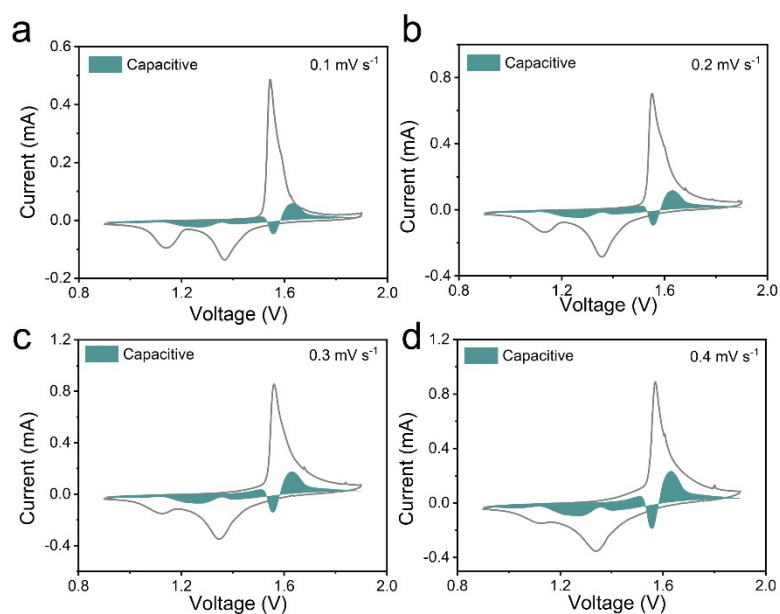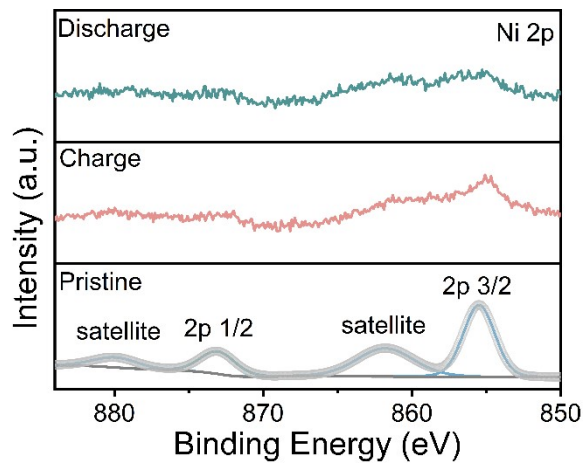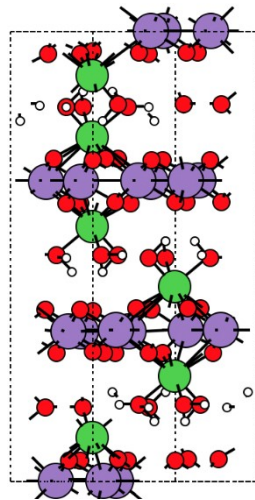**Fig.S19** GITT profiles of V_m-NMO and NMO.

Fig.S21 Capacitive contribution of NMO cathode material at various scan rates.

Fig. S22 Ex-situ Ni 2p XPS profiles of NMO cathode material in pristine, charge and discharge states.

Fig.S23 Structure model of $NiMn_3O_7 \cdot 3H_2O$.

Reference

1. Y. Zhang, H. Zhang, L. Fang, J. Deng and Y. Wang, *Electrochim. Acta.*, 2017, **245**, 32-40.
2. G. Held, F. Venturini, D. C. Grinter, P. Ferrer, R. Arrigo, L. Deacon, W. Quevedo Garzon, K. Roy, A. Large, C. Stephens, A. Watts, P. Larkin, M. Hand, H. Wang, L. Pratt, J. J. Mudd, T. Richardson, S. Patel, M. Hillman and S. Scott, *J. Synchrotron Radiat.*, 2020, **27**, 1153-1166.
3. Q. Li, X. Rui, D. Chen, Y. Feng, N. Xiao, L. Gan, Q. Zhang, Y. Yu and S. Huang, *Nano-Micro Lett.*, 2020, **12**, 67-67.
4. W. Weppner and R. A. Huggins, *J. Electrochem. Soc.*, 1977, **124**, 1569-1578.
5. Y. Zhu, T. Gao, X. Fan, F. Han and C. Wang, *Acc. Chem. Res.*, 2017, **50**, 1022-1031.
6. G. Kresse and J. Hafner, *Phys. Rev. B*, 1993, **47**, 558.
7. L. Bengtsson, *Phys. Rev. B*, 1999, **59**, 12301.
8. P. E. Blöchl, *Phys. Rev. B*, 1994, **50**, 17953.
9. J. P. Perdew, A. Ruzsinszky, G. I. Csonka, O. A. Vydrov, G. E. Scuseria, L. A. Constantin, X. Zhou and K. Burke, *Phys. Rev. Lett.*, 2008, **100**, 136406.
10. W. P. Davey, *Phys. Rev.*, 1925, **25**, 753.
11. J. Neugebauer and M. Scheffler, *Phys. Rev. B*, 1992, **46**, 16067.
12. S. Grimme, J. Antony, S. Ehrlich and H. Krieg, *J. Chem. Phys.*, 2010, **132**.
13. A. M. Ferrari, C. Pisani, F. Cinquini, L. Giordano and G. Pacchioni, *J. Chem. Phys.*, 2007, **127**.
14. C. Franchini, R. Podloucky, J. Paier, M. Marsman and G. Kresse, *Phys. Rev. B*, 2007, **75**, 195128.
15. W. Tang, E. Sanville and G. Henkelman, *J. Phys.: Condens. Matter.*, 2009, **21**, 084204.
16. K. Momma and F. Izumi, *J. Appl. Crystallogr.*, 2011, **44**, 1272-1276.
17. K. Momma and F. Izumi, *J. Appl. Crystallogr.*, 2008, **41**, 653-658.